Mechanism of the Gas-Phase HO + H_2O → H_2O + OH Reaction and Several Associated Isotope Exchange Reactions: A Canonical Variational Transition State Theory Plus Multidimensional Tunneling Calculation

Laura Masgrau, Angels González-Lafont, and José M. Lluch*

Departament de Química, Universitat Autònoma de Barcelona, 08193 Bellaterra, Barcelona, Spain

Received: September 17, 1998; In Final Form: December 8, 1998

Hydrogen abstraction from a molecule by OH is an important step in several reaction mechanisms of a key relevance in the chemistry of the atmosphere. The upper limit at 300 K for the rate constant of one of the simplest hydrogen abstraction reactions, HO + HOH → HOH + OH (1), has been experimentally established. This reaction is intrinsicaly interesting because the associated isotope exchange reactions, $H^{18}O$ + HOH → $H^{18}OH$ + OH (2) and DO + HOH → DOH + OH (3), could affect the isotopic composition of the stratospheric water. The rate constants for those two reactions have also been experimentally measured in the interval 300−420 K (reaction 2) and at 300 K (reaction 3). In addition, the upper limit at 300 K for the rate constant of the reaction HO + DOD → HOD + OD (4) has also been given. In this paper, we have theoretically calculated the rate constants and their temperature dependence for the above-mentioned four hydrogen (deuterium) transfer reactions by means of ab initio electronic structure calculations on their corresponding potential energy surfaces, followed by dynamical calculations based on the canonical unified statistical theory (CUS). The only available experimental activation energy (4.2 ± 0.5 kcal/mol for reaction 2 over the range 300−420 K) is in very solid agreement with our theoretical value of 4.27 kcal/mol obtained from first principles. In addition, our results confirm the experimental finding that these reactions have preexponential factors clearly lower than other typical hydrogen abstractions by HO. These low values for the two Arrhenius parameters come from a noticeable curved theoretical Arrhenius plot that, in turn, is a consequence of the large tunneling effects present in all these hydrogen (deuterium) abstraction reactions. No curvature was detected in the experimental Arrhenius plot for reaction 2, due to the small temperature range studied (300−420 K). The main cause for such large tunneling effects is the existence of an association complex, in which the two reactants are hydrogen bonded, which forms before the abstraction process itself takes place. Then, the adiabatic energy profile (effective potential for the tunneling calculation) is much thinner than that in a more typical bimolecular hydrogen (deuterium) transfer reaction. Finally, the kinetic isotope effects have been calculated, and a comparison with experimental rate constants rations has also been made.

Introduction

Hydroxyl radical HO is the predominant oxidant in the atmosphere. Therefore, hydrogen atom abstraction from a molecule by HO is an important step in the oxidation of organic compounds and in combustion systems, playing a key role in atmospheric chemistry.[1−4] Knowledge of the mechanisms and rate constants of those reactions is necessary for understanding and modeling many interrelated chemical processes that determine the quality of the environment supporting life on Earth.

On an initial assessment, the gas-phase radical-molecule identity reaction

$$HO + HOH \rightarrow HOH + OH \qquad (1)$$

is one of the simplest hydrogen abstraction reactions by the hydroxyl radical. This reaction is intrinsically interesting because the associated isotope exchange reactions

$$H^{18}O + HOH \rightarrow H^{18}OH + OH \qquad (2)$$

$$DO + HOH \rightarrow DOH + OH \qquad (3)$$

could affect the isotopic composition of the stratospheric water, a knowledge of which is useful to test the validity of several atmospheric models.[5]

Taking into account only the size of the system, reaction 1 is in effect a very simple process. However, the details of its mechanism are not completely understood yet. Dubey et al.[5] have very recently studied in a high-pressure flow reactor the isotope exchange reactions 2 and 3. They have reported a pressure-independent rate constant of $(2.2 \pm 1.0) \times 10^{-16}$ cm^3 molecule^{-1} s^{-1} for reaction 2 at 300 K, while they have measured a rate constant of $(3 \pm 1.0) \times 10^{-16}$ cm^3 molecule^{-1} s^{-1} for reaction 3. In addition, they have established an upper limit of 5×10^{-17} cm^3 molecule^{-1} s^{-1} for the rate of reaction 4 at 300 K.

$$HO + DOD \rightarrow HOD + OD \qquad (4)$$

Unfortunately, they did not measured the rate constant for reaction 1 because the kinetics measurements of such a reaction were blind to the formation of products due to the symmetry of this reaction. Dubey et al.[5] state that the similarity between the rates of reactions 2 and 3 indicates a small secondary isotope effect that they explain by means of arguments based on qualitative comparison of the zero-point energy correction at the reactants and the transition state.

10.1021/jp983749t CCC: $18.00
Published on Web 02/04/1999

Dubey et al.[5] have also measured the temperature dependence of the rate constant of reaction 2 from 300 to 420 K. Their results were fitted to a linear Arrhenius plot with a preexponential factor $A = (2.3 \pm 1.0) \times 10^{-13}$ cm^3 molecule^{-1} s^{-1} and an activation energy $E_a = 4.2 \pm 0.5$ kcal mol^{-1}. It is worth noting that we are dealing with hydrogen transfer reactions for which significant tunneling should be expected. Then the question is why no curvature can be viewed on the experimental Arrhenius plot.

An unclear point concerns the preexponential factor. The observed factor A for the reaction 2 is somewhat lower than values typical of hydrogen abstraction by HO (greater than 10^{-12} cm^3 molecule^{-1} s^{-1} or even 10^{-11} cm^3 molecule^{-1} s^{-1} over a similar range of temperatures[3,6−8]). Dubey et al.[5] attribute this fact to the existence of a complex in the entrance channel that poses an entropic constraint on the reaction probability. They propose that the evolution of reagent electronic interactions and geometrical transformations along the reaction path provide the entropic constraint. It seems then, that the above-mentioned complex plays an important role in determining the rate constant, even though it escapes direct observation during the reaction.

From the theoretical point of view, several authors[9−13] have used ab initio methods to locate minima with different geometries in several electronic states. Although two of them have turned out to be, in reality, transition states, it seems that the global minimum for the neutral $HO{\cdot}H_2O$ system has a C_s symmetry in a $^2A'$ electronic state, with hydrogen bonding occurring between the oxygen atom in the water molecule and the hydrogen atom in the hydroxyl radical. This global minimum (which would correspond to the above-mentioned complex) has a hydrogen bond distance H···O and a dissociation energy of 1.95 Å and 5.6 kcal mol^{-1}, respectively, at the restricted single and double excitation configuration interaction (RCISD), with the triple-ζ basis set of Huzinaga-Dunning augmented with two sets of polarization functions.[11]

On the other hand, Williams and co-workers[12] have used several different ab initio methods to calculate the barrier height for reaction 1. Their best estimate for the classical potential energy barrier was 12.9 kcal mol^{-1} at the basis set superposition error corrected, correlation energy scaled PUMP2/6-311++G(3d,2p)//UMP2/6-311G(d,p) plus an additional correction to provide an estimate for the result of a QCISD(T) computation. In turn, Dubey et al.[5] have found an adiabatic energy barrier (that is, including the zero-point energy corrections) of 19.2 kcal mol^{-1} for the reaction 1 at the UMP2/6-31G(d,p)//6-31G(d,p) level. They have carried out a linear least-squares fitting of experimental activation energies versus theoretical adiabatic energy barriers at this level of calculation for numerous hydrogen abstraction reactions, and as a result of this semiempirical correlation, they predict an experimental activation energy of 5 ± 1 kcal mol^{-1} for the reaction 1. Finally, and while this paper was being written, a second work by Williams and coworkers,[13] studying the kinetics of the perprotio reaction (reaction 1), appeared in the literature. In this work, the authors obtain a classical potential energy barrier for the symmetric hydrogen exchange of 10.1 and 9.9 kcal/mol at the QCISD(T)/6-311+G(3df,2p)//UMP2/6-31G(d) and G2 levels, respectively. The POLYRATE version 5.0.1[14] computer code was used to calculate temperature-dependent rate constants using variational transition state theory with multidimensional semiclassical tunneling corrections, and the minimum energy path required in these calculations was computed at the UMP2/6-311G(d,p) level. The theoretical rate constant value at 300 K reported by Williams and co-workers[13] is smaller than the experimental rate constant of reaction 2 by a factor of more than 300, leading to an activation energy, but in the temperature range 300−350 K, of 5.38 kcal/mol. After some energetic corrections, their best theoretical estimate for the Arrhenius activation energy at 300 K is of 5.07 kcal/mol. However, in the calculation of those rate constants for the perprotio reaction, the authors do not take into account the association complex that seems to exist on the potential energy surface.

The general purpose of this paper is the theoretical calculation of the rate constants of the identity reaction 1 and its isotopically substituted reactions 2−4, to identify the main factors that determine the mechanism of these hydrogen (deuterium) abstraction reactions. Specifically, we will focus on the role of the complex, the importance of tunneling, the calculation of the Arrhenius parameters, and the primary and secondary KIEs. Note that, because we take into account the existence of the complex, several dynamical bottlenecks to the reaction exist along the reaction path. As a consequence, we will have to perform a canonical unified statistical theory calculation. Our results can be particularly useful for reaction 1, for which no experimental rate constant has been measured, and for reaction 4, for which only an upper limit estimate of the rate constant exists.

Method of Calculation

In this section we will first describe the technical details corresponding to the electronic structure calculations and the dynamical treatment for the perprotio reaction. Finally, we will refer to the special calculations required to study the corresponding isotopically substituted reactions.

Electronic Structure Calculations. Geometries, energies, and first and second energy derivatives were calculated using the Gaussian 94[15] system of programs. We recall the general notation X//Y[16] to denote geometry optimization and Hessian evaluation (for frequencies) at level Y followed by a single-point energy calculation at level X. As usual, we omit //Y if Y is the same as X.

Stationary point geometries were optimized using the 6-311G(3d, 2p) basis set[17] (called B1 in this work) at the following levels: unrestricted Møller−Plesset second-order perturbation theory (UMP2),[16,18] density functional theory[19,20] with the three-parameter hybrid functional of Becke and the Lee, Yang, and Parr's correlation functional, which is widely known as B3LYP,[21,22] quadratic configuration interaction with single and double excitations (QCISD),[23] and coupled cluster including double (CCD) or single and double excitations (CCSD).[24,25] For the sake of comparison, the QCISD and CCSD stationary points were also localized using the 6-31G(d,p) basis set[16] (called B2 in this work). Harmonic vibrational frequencies were calculated at all the above-mentioned levels except for the CCSD/B1 level.

In addition, we carried out single-point energy calculations at the stationary points, at the following levels: QCISD(T)/B1//B3LYP/B1, CCSD(T)/B1//B3LYP/B1, PUMP2/B1//UMP2/B1, UMP4/B1//UMP2/B1, PUMP4/B1//UMP2/B1, QCISD(T)/B1//UMP2/B1, CCSD(T)/B1//UMP2/B1, QCISD(T)/B1//QCISD/B1, CCSD(T)/B1//CCSD/B1, where (T) stands for a perturbative estimate of the effect of triple excitations,[23,26−27] and PUMP2 and PUMP4 denote the spin projected UMP2 and UMP4 methods,[28] respectively. UMP4 calculations include the effects of single, double, triple, and quadruple excitations (SDTQ).

At this point, some results that will be discussed in the next section have to be introduced in order to understand the methodology we have employed. As both reactants approach each other, a first complex is formed, and then the hydrogen

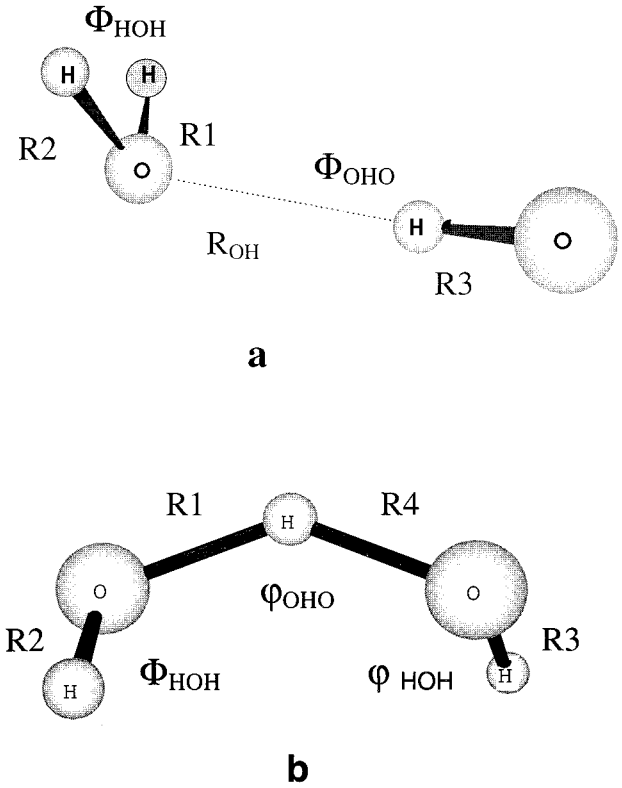

Figure 1. Definition of the geometrical parameters used in the text and in Table 1. a and b correspond to the complex C and saddle point structures, respectively.

abstraction itself occurs to reach a second complex, which finally dissociates toward the products. As a consequence, several regions can be distinguished along the reaction path, an association region from the reactants to the reactant complex (C), an abstraction region from the reactant complex (C) to the product complex (C′), and a dissociation region from the product complex (C′) to the products. Note that the reaction path for the perprotio reaction is symmetric.

In the association region, a distinguished reaction coordinate path (DCP) has been constructed by fixing the internuclear distance (R_{OH}; see Figure 1a) between the water oxygen atom and the hydrogen atom in the hydroxyl radical at different values and allowing the other degrees of freedom to relax. In this way, 31 DCP points have been obtained, ranging from $R_{OH} = 1.901$ Å (complex C) to $R_{OH} = 4.025$ Å at the UMP2/6-311G(3d, 2p) level. At each one of the DCP geometries, a generalized normal-mode analysis at the same level of theory has been performed in rectilinear coordinates.[29−32] Since in this region the minimum energy path[33,34] (MEP) has not been calculated, the use of the recently developed reoriented dividing surface (RODS)[35] algorithm becomes necessary in order to obtain reliable generalized eigenvectors and frequencies along the DCP path. Such generalized frequencies allow us to calculate the vibrationally adiabatic ground-state potential energy curve[31−33,36,37]

$$V_a^G(s) = V_{DCP,M}(s) + \epsilon^G_{tran}(s) \qquad (5)$$

where s denotes the distance along the DCP in an isoinertial mass-weighted coordinate system[30,31] (numerically equivalent to mass-scaled coordinates[33,34,36] with the scaling mass equal to 1 amu), $V_{DCP,M}(s)$ is the minimum classical energy in the reoriented dividing surface at s on the DCP, and $\epsilon^G_{tran}(s)$ is the zero-point energy (ZPE) at s from the generalized normal-mode vibrations transverse to the reaction path. For the aforementioned 31 points, we have also made single-point energy calculations at the CCSD(T)/B1//UMP2/B1/// level. (The X//Y/// notation[38] indicates single-point energy calculations at level X that are performed along the path calculated at level Y, not just at the stationary points).

Let us turn our attention at this point to the abstraction region of the potential energy surface (PES). As will be commented in the results section, in the UMP2/B1 PES two equivalent and relatively close saddle points appear (only 0.348 bohr apart), one on the reactant side and the other one on the product side. A very shallow minimum (M) separates those two saddle points. Starting from the UMP2/B1 reactant side saddle-point geometry, we have calculated the MEP and the classical energy along the minimum energy path, $V_{MEP}(s)$, where s here denotes the distance along the MEP in an isoinertial mass-weighted coordinate system, by following the Gonzalez−Schlegel mass-weighted internal coordinates reaction path algorithm[39] at the UMP2/Bl level. A gradient step size, δs, of 0.00529 Å (in mass-scaled coordinates with the scaling mass equal to 1 amu) was used to follow the MEP downhill enough to ensure, on one hand, that the minimum structure of complex C in Figure 1a connects with the saddle point of the hydrogen atom abstraction and on the other hand, to ensure convergence in the tunneling calculations that will be decribed in the next section. For 51 points along this MEP (reactant complex (C), saddle point, minimum (M), and 48 nonstationary points between C and M), we have also calculated the force constant matrix at the same UMP2/B1 level. As a result of the symmetry of the problem, the explicit calculation of the other moiety of the MEP has not been necessary. Then, a generalized normal-mode analysis was performed in rectilinear coordinates. The RODS algorithm has been used again in order to improve the generalized frequencies along the MEP. This allows us to calculate the vibrationally adiabatic potential energy curve corresponding to the abstraction region using eq 5, but substituting $V_{DCP,M}(s)$ by $V_{MEP,M}(s)$, $V_{MEP,M}(s)$ is the minimum classical energy in the reoriented dividing surface at s on the MEP. For the above-mentioned 51 points, we have also made single-point energy calculations at the highest level used in this work, obtaining improved values of $V_{MEP}(s)$ at the CCSD(T)/B1//UMP2/B1/// level.

As a result of the symmetry of the system, the electronic structure results of the dissociation region can be taken from the PES exploration of the association region.

Dynamical Calculations. Since two complexes C and C′ appear along the reaction path, there are three dynamical bottlenecks in the reaction: (a) in the association region; (b) in the abstraction region; (c) in the dissociation region. The rate constants for passage through these three bottleneck regions will be labeled k_{as}, k_{ab}, and k_{di}, respectively. k_C and $k_{C'}$ will denote the one-way flux rate constants evaluated at the C and C′ complexes, respectively.

According to the canonical unified statistical theory (CUS),[32,40−41] the final reaction rate constant $k(T)$ is given by

$$\frac{1}{k(T)} = \frac{1}{k_{as}(T)} - \frac{1}{k_c(T)} + \frac{1}{k_{ab}(T)} - \frac{1}{k_{C'}(T)} + \frac{1}{k_{di}(T)} \qquad (6)$$

The k_{as}, k_{ab}, and k_{di} rate constants were calculated by direct multidimensional semiclassical dynamics, that is, including multidimensional quantum effects on the nuclear motion (when necessary) by a semiclassical method and obtaining all required information about the potential energy surface directly from electronic structure calculations, without the intermediacy of an analytic potential energy function. Canonical variational transition state theory (CVT)[30−32,36,37,42−44] rate constants and

TABLE 1: Ab Initio Geometries (Distances in Å and Angles in Degrees)[a]

	coordinate	B3LYP/B1	UMP2/B1	QCISD/B2	QCISD/B1	CCD/B1	CCSD/B2	CCSD/B1
H_2O	$R1 = R2$	0.961	0.956	0.976	0.955	0.954	0.976	0.955
	Φ_{HOH}	104.0	103.4	109.2	103.7	103.9	109.1	103.8
OH	$R3$	0.974	0.965	0.997	0.967	0.965	0.997	0.967
complex C	$R1 = R2$	0.962	0.958	0.974	0.956	0.954	0.974	0.956
	$R3$	0.982	0.971	1.001	0.971	0.969	1.000	0.971
	R_{OH}	1.891	1.901	1.871	1.925	1.913	1.871	1.925
	Φ_{HOH}	104.8	104.3	110.4	104.6	105.3	110.4	104.7
	Φ_{OHO}	172.6	174.7	180.0	174.5	180.0	180.0	178.0
saddle point	$R1$	1.165	1.108 (1.143)	1.193	1.159	1.147	1.190	1.158
	$R4$	1.165	1.190 (1.143)	1.193	1.159	1.147	1.190	1.158
	$R2$	0.964	0.964 (0.964)	0.987	0.963	0.961	0.987	0.963
	$R3$	0.967	0.964 (0.964)	0.987	0.963	0.961	0.987	0.963
	Φ_{HOH}	103.2	101.9 (102.7)	106.5	101.4	102.2	106.7	101.4
	φ_{HOH}	103.2	101.8 (102.7)	106.5	101.4	102.2	106.7	101.4
	φ_{OHO}	142.5	139.2 (138.5)	138.3	140.9	143.2	138.9	141.5
	ω	63.4	58.0 (59.4)	61.1	59.5	56.5	59.6	58.8

[a] For definition of acronyms see Method of Calculation section.

semiclassical transmission coefficients[42,43,45] were calculated using version 7.9.1 of the POLYRATE computer program.[46,47] Bound vibrational and rotational motions were assumed to be separable, and the vibrational partition functions were computed quantum mechanically within the harmonic approximation. The reaction path symmetry factor σ has been included in the calculations of the rate constants ($\sigma = 2$ for all our cases). An interpolation scheme[48] based on a spline fitting of the reaction path data was used to obtain properties (geometry, classical energy, and generalized normal-mode frequencies) at every 0.010 58 Å along the path from complex C to complex C′ in the abstraction region. As for the association region (and taking into account the symmetry properties, as is also the case for the dissociation region), a four-point Lagrange interpolation has been performed from $R_{OH} = 1.901$ Å (complex C) up to $R_{OH} = 4.025$ Å; from this point to reactants, the classical energy and the zero-point energy corrections have been extrapolated. The generalized free energy of activation was then calculated at each of these points, and the location of the variational transition state and the CVT rate constants were determined by interpolating to the maximum of this function for each temperature. Frequencies between consecutive points along the reaction path were correlated adiabatically.[31,49]

Quantum mechanical tunneling effects (when necessary) were included by multiplying the CVT rate constants by a transmission coefficient $\kappa(T)$. The small-curvature tunneling (SCT) semiclassical adiabatic ground-state approximation has been employed.[50,51] This approximation is a multidimensional tunneling method because V_a^G includes the variation with s of the zero-point energy of all eight vibrational modes that are orthogonal to the reaction coordinate.

To ensure convergence of the calculated rate constants, preliminary rate calculations with coarse Hessian grids were used to locate the regions of the reaction path containing the temperature-dependent variational transition states and the minima of the SCT reduced mass, where the "corner cutting" aspect of the tunneling process would be greatest. Finer grids were then calculated for these critical regions to improve the accuracy of the calculated canonical rate constants and small-curvature tunneling probabilities, resulting finally in the 31 and 48 nonstationary Hessian grid points mentioned above. This strategy is sometimes called focusing.[52]

The one-way flux rate constants, k_C and $k_{C'}$, were variationally estimated by minimizing the free energy in the proximity of the complexes C and C′.

Isotopically Substituted Reactions. The general methodology we have used for the isotopically substituted reactions is the same as the one followed for the perprotio reaction, although some differences appear. By definition, the MEP depends on the atomic masses of the atoms involved in the reaction, and therefore, for each isotopic substitution a new MEP must be calculated. However, under the Born−Oppenheimer approximation, the potential energy surface of the system is independent of the atomic masses. Since the RODS method has been developed for computing CVT rate constants including multidimensional tunneling contributions without having to evaluate the MEP for each isotopically substituted reaction, the perprotio MEP has been taken as the reaction path for the isotopically substituted reactions in the abstraction region. Note that the DCP is independent of the masses of the atoms. However, due to the different isotopic distribution in the reactant and product regions of the isotopically substituted reactions, the generalized normal-mode vibrations transverse to the reaction path in the association region are different from the ones corresponding to the dissociation region. Then, for the isotopically substituted reactions, these two regions have to be explicitly studied.

TABLE 2: Energies (kcal/mol) of the Stationary Points for the HO + HOH → HOH + OH Reaction[a]

method[b]	V_C	$V^{\ddagger}$	$(\Delta V_a^G)_C$	$\Delta V_a^{G\ddagger}$
B3LYP/B1	−8.0	−1.1	−5.7	−1.3
UMP2/B1	−8.0	10.4 (10.2)	−5.7	10.5 (13.6)
QCISD/B2	−9.1	11.8	−6.6	11.6
QCISD/B1	−7.5	11.2	−5.1	10.9
CCD/B1	−7.0	15.3	−5.1	15.0
CCSD/B2	−9.1	12.5	−6.6	12.5
CCSD/B1	−7.4	11.9		

[a] V_C is the classical energy of complex C; $V^{\ddagger}$ is the classical energy barrier (the value in parentheses is the classical energy of minimum M); $(\Delta V_a^G)_C$ is the adiabatic depth of complex C; $\Delta V_a^{G\ddagger}$ is the adiabatic energy barrier (the value in parentheses is the adiabatic energy of minimum M with respect to the reactants). [b] See Method of Calculation section.

Results and Discussion

In this section, we will first present the results corresponding to the electronic structure calculations on the HO + HOH → HOH + OH reaction. The dynamical results for the perprotio and the isotopically substituted reactions will be also described.

Electronic Structure Calculations. The optimized geometries for the stationary points of the perprotio reaction are presented in Table 1. Table 2 summarizes the results for the energetics of the stationary points of this reaction. The general

picture of the perprotio reaction pathway has already been described in the previous section. We have pointed out that it is a reaction that takes place through several dynamical bottlenecks. Initially, there is the association of the two reactants, followed by the hydrogen abstraction process within the complex formed, which finally dissociates into the two separated products. In the association region, the hydroxyl radical and the water molecule approach each other giving rise to the hydrogen-bonded complex C (depicted in Figure 1a) with neither a classical nor an adiabatic energy barrier at the UMP2/B1 and CCSD(T)/B1//UMP2/B1 levels. The hydrogen bonding in complex C occurs between the H atom of the hydroxyl radical and the oxygen atom in water. From an inspection of Table 1, it can be observed that the geometry parameters are quite stable throughout the different levels of theory, though the R_{OH} distance tends to increase slightly as the basis set is extended and as correlation effects are taken into account. The linearity of the hydrogen bond decreases as the basis set is extended and when single excitations are included in the coupled cluster optimization with the B1 basis set. Regarding the energetics of complex C (see Table 2), we have achieved a result in which the well depth in classical energy for the association process decreases as the basis set is extended. Using the B1 basis set, the stabilization in terms of classical energy is of -7.0 kcal/mol to -8.0 kcal/mol at the five levels of calculation used in this work. The minimum energy structure C corresponds to a $^2A'$ electronic state with C_s symmetry. In a previous theoretical study by Xie and Schaeffer,[11] it was found (at different levels of calculation than those used here) that the global minimum of the H_3O_2 system was a $^2A'$ state with C_s symmetry, in accordance with our calculations. In addition, Williams et al.[13] also agree in their most recent work about the structure and electronic state of the global minimum of this association complex, although they state that the encounter complex relevant to hydrogen atom abstraction from molecules HOR by radicals R′O is not this global minimum structure but the species HO···HOH, in which the hydrogen bond donor is the water molecule instead of the hydroxyl radical. The adiabatic well depths $(\Delta V_a^G)_C$, evaluated at complex C (third numerical value in Table 2) are less negative than the corresponding classical stabilization energies at all the levels of calculation. As the basis set is extended, $(\Delta V_a^G)_C$ becomes even less negative. With the B1 basis set, the final $(\Delta V_a^G)_C$ value calculated at the four correlated levels for which we have frequencies ranges from -5.1 to -5.7 kcal/mol.

The abstraction process from reactant complex C to the symmetric product complex C′ takes place with a positive classical energy barrier with respect to reactants. The saddle point for the symmetric hydrogen atom transfer (depicted in Figure 1b) has C_2 symmetry at all the levels of calculation used in this work except for the UMP2/B1 level. The abstraction saddle point geometrical parameters are also presented in Table 1. The agreement between the different methodologies, apart from the UMP2/B1 calculation, is quite good. The smaller B2 basis set, though, gives longer R_1 distances. On the UMP2/B1 potential energy surface, there are two asymmetric saddle points, one on the reactant side and the other on the product side, equivalent to each other and separated by a shallow minimum M. The R_1 and R_4 distances at those two UMP2/B1 saddle points are 1.108 and 1.190 Å, whereas both distances become equal (1.143 Å) at the C_2 minimum energy structure M, whose geometrical parameters are given in parentheses in Table 1. In fact, the minimum energy structrure M on the UMP2/B1 PES corresponds to the saddle point geometry for the hydrogen transfer found at the other levels of calculation. Williams and co-workers[12] had already located the C_2 structure for the perprotio reaction at UMP2 level, though using different basis sets, and in the most recent work of Williams and co-workers,[13] the authors have characterized it as a minimum (instead of as a saddle point) and have found the true saddle point with asymmetric geometry on two UMP2 PES different from ours. The classical and adiabatic energy barriers for the hydrogen abstraction process are given in Table 2. The values in parentheses correspond to the energy differences with respect to reactants evaluated at structure M at UMP2/B1 level. The classical energetic difference between the asymmetric saddle point and the minimum M at the UMP2/B1 level is not significant (0.2 kcal/mol). The UMP2/B1 classical energy barrier is somewhat smaller than the QCISD/B1 and CCSD/B1 barriers. The use of a smaller basis set tends to increase the classical barrier as well as if single excitations are not included in the coupled cluster calculation. The B3LYP methodology gives a negative classical barrier for the hydrogen-transfer process. The adiabatic energy barrier ($\Delta V_a^{G\ddagger}$) at the UMP2/B1 level is close to the QCISD/B1 result, whereas a smaller basis set and the CCD calculations give higher barriers and the B3LYP methodology results in a negative adiabatic energy barrier. The difference in the ΔV_a^G values between the UMP2/B1 saddle point and the minimum energy structure M is more important because there is a significant decrease of the vibrational frequencies in going from M to the UMP2 saddle point. The hydrogen-transfer movement of high frequency that describes the MEP at the saddle point becomes a movement orthogonal to this MEP when approaching the minimum M, thus increasing the zero-point energy contribution along the path. In contrast, the main components of the gradient along the MEP in the shallow minimum's region correspond to oxygen atom displacements and correlate with the components of a low-frequency mode at M. It must also be taken into account that in the ΔV_a^G value at M in Table 2 there is one more degree of freedom contributing to the zero-point energy than at the saddle point.

TABLE 3: Single-Point Energy Calculations[a]

method[b]	V_C	$V^{\ddagger}$
QCISD(T)/B1//B3LYP/B1	−7.7	8.7
CCSD(T)/B1//B3LYP/B1	−7.7	9.0
PUMP2/B1//UMP2/B1	−8.0	7.3 (6.4)
UMP4/B1//UMP2/B1	−7.9	9.4 (9.4)
PUMP4/B1//UMP2//B1	−7.8	7.8 (7.6)
QCISD(T)/B1//UMP2/B1	−7.8	8.3 (8.7)
CCSD(T)/B1//UMP2/B1	−7.8	8.6 (9.0)
QCISD(T)/B1//QCISD/B1	−7.8	8.4
CCSD(T)/B1//CCSD/B1	−7.7	8.8
CCSD(T)/B1//UMP2/B1///	−7.8	8.6 (9.0)

[a] V_C is the classical energy of complex C; $V^{\ddagger}$ is the classical energy barrier (the values in parentheses are the classical energies of minimum M). [b] See method of calculation section.

Table 3 summarizes the single-point classical energy calculations performed in this work. The second numerical column gives the classical stabilization energies of complex C (V_C), the third numerical column presents the classical energy barriers ($V^{\ddagger}$) of the abstraction process evaluated at different saddle-point geometries, and the values in parentheses are single-point energy calculations at the M structure of the UMP2/B1 PES. The last row of Table 3 shows the results of carrying out higher level single-point energy calculations along the UMP2/B1 path and finding the minimum and maximum potential along the path. The V_C values agree within 0.3 kcal/mol along the whole series of single-point energy calculations. The inclusion of triples at the QCISD and CCSD levels only slightly stabilizes complex C (see Table 2 for comparison). At the UMP2/B1 saddle-point

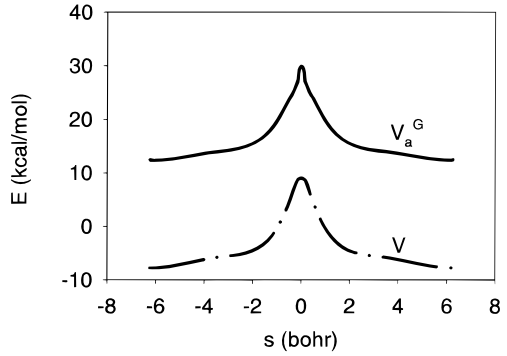

Figure 2. Classical energy curve (V) and adiabatic potential energy curve (V_a^G), with respect to the classical energy of reactants separated at infinite distance, as a function of s along the MEP connecting C and C′ in the abstraction region for the perprotio reaction. Note that at reactants V_a^G is 18.8 kcal/mol.

geometry, the energy calculation at higher levels of theory always results in a lowering of the classical potential energy barrier. In particular, the approximate spin projection techniques PUMP2 and PUMP4 lower the abstraction barrier by 3.1 and 2.6 kcal/mol, respectively, which indicates a spin contamination ($\langle S^2 \rangle = 0.79$) problem in the unrestricted Moller−Plesset wave functions. At the QCISD(T)/B1//UMP2/B1 and CCSD(T)/B1//UMP2/B1 levels, the classical energy maximum moves toward the M structure of C_2 symmetry, in agreement with the fully optimized geometry at the QCISD/B1 and CCSD/B1 levels (see Table 1 for comparison). These two calculations at the QCISD(T) and CCSD(T) levels on the UMP2/B1 geometries for structure M, giving values of 8.7 and 9.0 kcal/mol, respectively, agree very well with the corresponding $V^{\ddagger}$ single-point energy values at the QCISD(T)/B1//QCISD/B1 (8.4 kcal/mol) and the CCSD(T)/B1//CCSD/B1 (8.8 kcal/mol) levels. These results, the geometries compared in Table 1 and the energetics of Table 2, suggest that, although it is not quite adequate from an energetic perspective, the UMP2/B1 level may be useful for providing a reaction path for the HO + HOH → HOH + OH reaction. This conclusion had already been achieved by Williams and co-workers.[12−13]

The dynamical calculations were then based on a UMP2/B1 reaction path consisting of a distinguished-coordinate path (DCP) in the association and dissociation regions and on a minimum-energy path (MEP) in the abstraction region. The energy profile along the reaction path was corrected by performing single-point energy calculations at the CCSD(T)/B1 level. As already mentioned, this type of calculation will be called CCSD(T)/B1//UMP2/B1///. The agreement between the V_C and $V^{\ddagger}$ values at the CCSD(T)/B1//UMP2/B1/// and CCSD(T)/B1//UMP2/B1 levels (see Table 3) indicates that there is no displacement of the minimum and maximum of the CCSD(T)/B1//UMP2/B1/// curve from the UMP2/B1 geometries for complex C and structure M.

Dynamical Calculations. The classical energy curve (V) as a function of s along the MEP connecting C and C′ in the abstraction region is plotted in Figure 2 at the CCSD(T)/B1//UMP2/B1/// level for the HO + HOH → HOH + OH reaction. The zero of energy is given by the two reactants separated at infinite distance, and the origin of variable s is taken at the estimated location of the saddle point for the hydrogen-transfer process. As indicated above, the saddle point location is estimated by finding the highest CCSD(T)/B1//UMP2/B1/// energy along the path and, in this case, coincides with the geometry for the M structure on the UMP2/B1 PES. Along with the $V(s)$ curve, the $V_a^G(s)$ values are also included in Figure 2

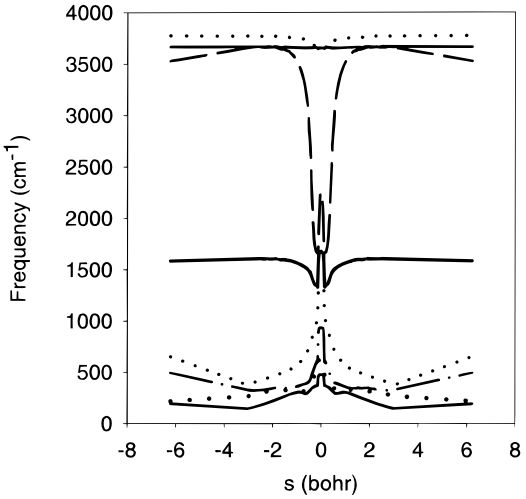

Figure 3. Generalized frequencies as a function of s along the MEP connecting C and C′ in the abstraction region for the perprotio reaction.

in the same range of s. The plot shows that the $V_a^G(s)$ curve in the abstraction region is very narrow around $s = 0$ because there are several frequencies that significantly increase their values from $s = \pm 0.14$ bohr to $s = 0$, location where all those frequencies reach a maximum (see Figure 3). It is important to indicate here that, in accordance with the recommendations of Scott and Radom,[53] in all our dynamical calculations the UMP2/B1 frequencies have been scaled by a factor of 0.9496. The $V(s)$ and $V_a^G(s)$ curves in the association and dissociation regions are not included in Figure 2. Neither of these two curves present an energetic maximum, so both curves monotonically decrease from reactants to complex C and monotonically increase from complex C′ up to products. At $T = 0$ K, the entropic contributions and the thermal corrections to the Gibbs activation free energy vanish and, consequently, $\Delta V_a^G(s) = \Delta G^{GT,\circ}(s)$. As T increases, our results show that there is no variational effect in the abstraction region; that is, the maximum of the $\Delta G^{GT,\circ}(s)$ profile does not shift from the $s = 0$ location in the whole temperature range studied. In constrast, in the association region the $-T\Delta S^{GT,\circ}(s)$ term moves the variational transition state from its initial location at reactants at $T = 0$ K toward complex C as T grows. Analogously, there is a variational displacement of the transition state in the dissociation region from products to complex C′. On the other hand, no significant chemical differences related with the $\Delta G^{GT,\circ}(s)$ curves have been found for the isotopically substituted reactions.

Table 4 lists the variational rate constant values as a function of temperature for the perprotio reaction as well as for the isotopically substituted reactions. k_{as}^{CVT} stands for the CVT association rate constants. k_{ab}^{CVT} and $k_{ab}^{CVT/SCT}$ stand for the CVT rate constants and CVT with SCT tunneling correction rate constants of the abstraction process, respectively. k_{di}^{CVT} refers to the CVT dissociation rate constants. We will comment first on the rate constants for the HO + HOH → HOH + OH (1) reaction, and then we will compare with the dynamical results of the isotopically substituted reactions 2−4.

As expected, the association and dissociation rate constants for the perprotio reaction are identical due to the symmetry of the system. Both rate constants change slightly as temperature increases, but in the whole temperature range analyzed, the k_{as}^{CVT} and k_{di}^{CVT} figures are on the order of 10^{-10}, being clearly bigger than the corresponding abstraction rate constants at each temperature. No tunneling correction contributes to the association and dissociation rate constants because, as we have already explained, there is no adiabatic barrier in those two regions.

TABLE 4: Rate Constants (in cm^3 molecule^{-1} s^{-1}) at Several Temperatures (Power of 10 in Parentheses)

T (K)	k_{as}^{CVT}	k_{ab}^{CVT}	$k_{ab}^{CVT/SCT}$	k_{di}^{CVT}
		HO + HOH = HOH + OH (1)		
200	3.71(−10)	6.78 (−25)	1.70(−18)	3.71(−10)
300	3.70(−10)	7.77(−21)	1.82(−17)	3.70(−10)
400	4.27(−10)	8.26(−19)	1.08(−16)	4.27(−10)
500	5.14(−10)	1.40(−17)	4.04(−16)	5.14(−10)
700	7.60(−10)	3.88(−16)	2.55(−15)	7.60(−10)
		$H^{18}O$ + HOH = $H^{18}OH$ + OH (2)		
200	3.67(−10)	7.12(−25)	2.18(−18)	3.88(−10)
300	3.64(−10)	7.96(−21)	2.16(−17)	3.78(−10)
400	4.20(−10)	8.31(−19)	1.25(−16)	4.31(−10)
500	5.07(−10)	1.40(−17)	4.57(−16)	5.16(−10)
700	7.49(−10)	3.88(−16)	2.77(−15)	7.57(−10)
		DO + HOH = DOH + OH (3)		
200	3.62(−10)	1.09(−24)	2.14(−18)	8.77(−10)
300	3.40(−10)	9.52(−21)	1.79(−17)	6.06(−10)
400	3.82(−10)	8.97(−19)	9.76(−17)	5.91(−10)
500	4.54(−10)	1.42(−17)	3.50(−16)	6.48(−10)
700	6.63(−10)	3.73(−16)	2.15(−15)	8.70(−10)
		HO + DOD = HOD + OD (4)		
200	5.20(−10)	5.04(−25)	1.73(−20)	2.04(−10)
300	4.35(−10)	5.23(−21)	7.12(−19)	2.37(−10)
400	4.70(−10)	5.45(−19)	9.53(−18)	2.99(−10)
500	5.48(−10)	9.28(−18)	6.07(−17)	3.80(−10)
700	7.87(−10)	2.70(−16)	7.25(−16)	5.97(−10)

Regarding the dynamical results of reaction 1 for the hydrogen-transfer event, we infer from the data in Table 4 that the k_{ab}^{CVT} rate constants significantly increase as T grows.The tunneling correction, evaluated by means of the SCT methodology, is quite important in the whole temperature range, thus contributing to an increase in the abstraction rate constants, especially at the lower temperatures. The final rate constants for reaction 1 would be given by eq 6 according to the CUS theory, which takes into account the appearance of multiple dynamical bottlenecks in an activation free energy profile. However, as k_{as}^{CVT} and k_{di}^{CVT} are very big in comparison with $k_{ab}^{CVT/SCT}$, the contribution of those two former rate constants to the final value of $k(T)$ is negligible. Note that these rate constants correspond to k_{as}, k_{di}, and k_{ab}, respectively, in eq 6. In addition, we have estimated the k_C and $k_{C'}$ values (one-way flux rate constants evaluated at C and C′) and their order of magnitude is around 10^{-7} cm^3 molecule^{-1} s^{-1} at 300 K. Obviously then, their contribution to the final $k(T)$ rate constant is completely insignificant. Accordingly, the final CUS rate constant $k(T)$ of eq 6 is reduced to its single important contribution in the range 200−700 K, namely, the $k_{ab}^{CVT/SCT}$ rate constant. At much higher temperatures and due to the rapid increase of $k_{ab}^{CVT/SCT}$ with temperature the hydrogen transfer rate constant might become of the same order of magnitude as k_{as}^{CVT} and k_{di}^{CVT}. In that case, the three rate constants should be considered in using eq 6.

As for the isotopically substituted reactions, it is worth noting that the k_{as}^{CVT} rate constants are no longer the same as the k_{di}^{CVT} rate constants, because of the different isotopic distributions in the reactant and the product regions. In any case, as before, all the k_{as}^{CVT} and k_{di}^{CVT} rate constants are of the order of 10^{-10} in the whole temperature range, and for that reason, they do not have any significant weight in the final value of $k(T)$ (eq 6).

Concerning the isotopically substituted k_{ab}^{CVT} rate constants, we see that from 200 to 500 K reaction 3 is faster than reaction 2 and reaction 2 is faster than reaction 1. This order is in agreement with the arrangement of adiabatic barriers (11.35 kcal/mol (3), 11.69 kcal/mol (2), and 11.72 kcal/mol (1)) and with the explanation based on zero-point energy effects reported by Dubey et al.[5] to rationalize their experimental results. The k_{ab}^{CVT} rate constants for reaction 4 are the smallest in the whole temperature range mainly due to entropic effects. When tunneling is included by means of the SCT transmission coefficient, the order of rate constant values among the different reactions changes somewhat. Reaction 2 becomes the fastest, whereas reaction 4 remains as the slowest from 200 to 700 K because the correction by tunneling is smaller when a deuterium atom transfers instead of a protium atom. From 300 to 700 K, reaction 1 and reaction 3 exchange positions because the SCT tunneling correction is more important for reaction 1.

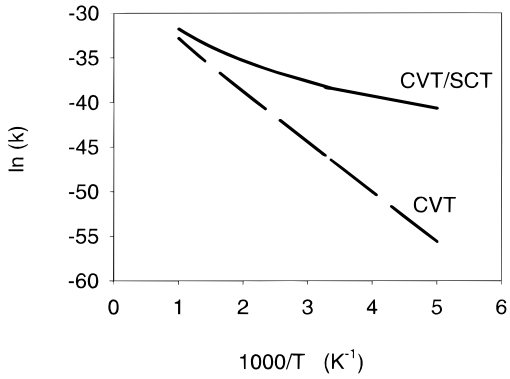

Figure 4. Arrhenius plots corresponding to the k_{ab}^{CVT} (dashed line) and $k_{ab}^{CVT/SCT}$ (solid line) rate constants (in cm^3 molecule^{-1} s^{-1}) for reaction 2.

Besides the differences in the transmission coefficient values of the four studied reactions, the most remarkable conclusion we can draw from the comparison of the data in Table 4 is that tunneling is very important in these hydrogen (deuterium) transfer processes at 300 K and even at higher temperatures. Why are tunneling contributions to the rate constants so important in these reactions? The main cause for those large tunneling effects is the existence of complex C. The adiabatic energy profiles for the bimolecular hydrogen (deuterium) transfer processes without passing through the formation of the association complex C would be wider than the ones we obtain and, consequently, the tunneling effects would be smaller. In other words, the distances between classical turning points are very small, even at the lowest energy level available for tunneling. As a result of the previously formed complex C, when tunneling in the abstraction process begins to occur, the most important movement of the two oxygens (heavy atoms) approaching each other from infinity has already taken place along the reaction path and, although there is still a small approximation of those two heavy atoms up to the transition state, the main contributions to the tunneling paths come from hydrogen (or deuterium) motions. In Figure 4, the Arrhenius plots corresponding to the k_{ab}^{CVT} and $k_{ab}^{CVT/SCT}$ rate constants for reaction 2 are depicted. The curvature of the Arrhenius plot is noticeable when tunneling is included in the calculation if a large temperature range is considered (200−1000 K), thus confirming the importance of tunneling effects in those reactions. On the other hand, it is also clear that a nearly linear Arrhenius plot would apparently result if only our calculated $k_{ab}^{CVT/SCT}$ rate constants in the small experimental temperature range (300−420 K) were represented versus T^{-1}. This fact allows us to understand why no curvature on the experimental Arrhenius plot was detected by Dubey et al.[5] in this reduced range of temperatures.

Let us turn our attention to the Arrhenius parameters that can be deduced from our calculations for the four reactions. The preexponential factors and activation energies at 300 K,

TABLE 5: Preexponential Factors (in cm^3 molecule^{-1} s^{-1}) and Activation Energies (in kcal/mol) at Several Temperatures (Power of 10 in Parentheses)

	300 K		300−420 K		700 K	
	A	E_a	*A*	E_a	*A*	E_a
(1) HO + HOH = HOH + OH	9.41(−15)	3.73	2.62(−14)	4.34	4.98(−10)	7.27
(2) $H^{18}O$ + HOH = $H^{18}OH$ + OH	1.04(−14)	3.68	2.81(−14)	4.27	4.17(−10)	7.11
(3) DO + HOH = DOH + OH	6.27(−15)	3.49	1.81(−14)	4.13	4.02(−10)	7.24
(4) HO + DOD = HOD + OD	7.67(−15)	5.54	2.70(−14)	6.29	5.00(−09)	9.50

over the range 300−420 K, and at 700 K are presented in Table 5. Activation energies are obtained from rate constants through the usual definition

$$E_a = -R\frac{d(\ln k(T))}{d(1/T)} \quad (7)$$

which is equivalent to determining the slope of the plots as the one shown in Figure 4 for reaction 2. Each preexponential factor corresponds to the value at which the straight line tangent to the plot intercepts the ln *k* axis at infinite temperature. As expected, the slopes of the plots, and therefore the activation energies, increase as tunneling becomes less dominant at higher temperatures. Reaction 4, which transfers a deuterium atom, has less tunneling and, as a consequence, approaches the classical Arrhenius behavior more rapidly as the temperature grows, in this way giving activation energies clearly greater than those of the other three reactions (which are all very similar) at all temperatures studied. When comparing with the only available experimental activation energy (4.2 ± 0.5 kcal/mol for reaction 2 over the range 300−420 K), the agreement with our theoretical value (4.27 kcal/mol) is excellent. Note that this theoretical value has been obtained from first principles, with no semiempirical correlation as that done by Dubey et al.[5] (as mentioned in the Introduction) having been performed.

On the other hand, the preexponential factors depend on the balance between two factors, the rate constant and the slope of the Arrhenius plot at the corresponding temperature. As seen in Table 5 for reactions 1−3, in the range of temperatures where tunneling is significant (low slope), the *A* parameters tend to keep the order of the rate constants themselves (in fact, at the limit of very low temperatures leading to the region of nearly activationless reactions, the preexponential factor becomes ever closer to the rate constant itself). As the temperature augments, the slopes of the curves also increase; the values of the intersections at infinite temperature become higher and lose the memory of the rate constant values at the considered temperature. Since the particular region of temperatures in which the transition from quantum to more classical behavior of the Arrhenius plot occurs depends on each reaction, some crossings can take place. Thus, the preexponential factor of reaction 4 becomes progressively the greatest as the temperature increases, although the corresponding rate constant is always the smallest among the four reactions (see Table 4) over the range of considered temperatures. This reflects the fact that, as mentioned above, reaction 4 approaches the classical Arrhenius behavior more rapidly. As for the comparison with the experimental result for the reaction 2 over the range 300−420 K, our corresponding theoretical preexponential value (2.81×10^{-14} cm^3 molecule^{-1} s^{-1}) is acceptable, although it turns out to be somewhat smaller.

Our results confirm the experimental finding that these reactions have preexponential factors clearly lower than those of other typical hydrogen abstractions by HO. The advantage of our theoretical calculations is that we are able to analyze the main reason for this. Connecting the Arrhenius equation with the quasithermodynamic formulation of the transition state theory, as is well-known, the preexponential factor exponentially depends on the phenomenological activation entropy of the reaction $\Delta S^{\circ\ddagger}$. According to Truhlar and Garrett,[54] this term can be partitioned into substantial ($\Delta S_s^{\circ\ddagger}$) and nonsubstantial ($\Delta S_n^{\circ\ddagger}$) contributions. The former derives from properties of a single temperature-independent transition state by conventional methods. The nonsubstantial contributions arise from the dependence of the variational transition state on temperature and tunneling effects. In this paper, we have obtained both contributions for reaction 2 at 300 K. The decomposition (by using the van't Hoff equation) of the substantial Gibbs activation free energy into the corresponding substantial enthalpic and entropic contributions leads to the values 9.96 kcal/mol and −22.26 cal mol^{-1} K^{-1} for $\Delta H_s^{\circ\ddagger}$ and $\Delta S_s^{\circ\ddagger}$, respectively. Incidentally, note that, due to a significant contribution of tunneling, the substantial activation enthalpy is much greater than the corresponding activation energy (3.68 kcal/mol in Table 5). Considering that the dependence of the variational transition state on the temperature is, in practice, negligible for reaction 2, the nonsubstantial entropic term comes entirely from tunneling here. So calculation of the transmission factor and its derivative with respect to the temperature gives $\Delta S_n^{\circ\ddagger} = -9.19$ cal mol^{-1} K^{-1}, which leads to $\Delta S^{\circ\ddagger} = -31.45$ cal mol^{-1} K^{-1}. Thus, tunneling is responsible for 29% of the phenomenological activation entropy of reaction 2 at 300 K. In other words, the additional entropic constraint introduced by the tunneling reduces the preexponential factor by 2 orders of magnitude. In this sense, the existence of the complex, which causes an important enhancement of tunneling, is decisive in order to have such a small preexponential factor, with no additional electronic or geometrical considerations being necessary to explain it.

Another point concerns the kinetic isotope effects. KIEs are defined as the ratios k_1/k_i ($i = 2-4$), where k_1 is the rate constant for the unsubstituted reaction 1 and k_i stands for the rate constants of the isotopically substituted reactions 2−4. Reaction 3 involves a secondary H/D KIE, while reaction 4 implies a primary H/D KIE. We think that the $^{16}O/^{18}O$ KIE associated with reaction 2 is primary rather than secondary, as stated by Dubey et al.[5] By definition, a KIE is normal if it is greater than unity when the rate constant for the lighter isotope is in the numerator, and it is an inverse isotope effect if it is less than unity. In Table 6 we present the theoretical rate constants and KIEs along with the experimental rate constants at 300 K. We have not given the experimental KIEs because the experimental rate constant for reaction 1 has not been measured. Although our theoretical values for reactions 2 and 3 are somewhat lower than the experimental ones, our results are quite good, internally very consistent, and provide concrete (and plausible) rate constants for reactions 1 and 4. Reaction 2 has a slight inverse primary KIE, whereas the normal secondary KIE of reaction 3 turns out to be nearly negligible. Conversely, reaction 4 exhibits an extremely large normal primary KIE that is a direct consequence of a significant quenching of tunneling due to the substitution of the shifting hydrogen by deuterium. For the sake of comparison with the experimental rates, we can see that our

TABLE 6: Rate Constants (in cm^3 molecule^{-1} s^{-1}) and Kinetic Isotope Effects at 300 K (Power of 10 in Parentheses)

	k			KIE	
	theor	theor scaled	exp[a]	theor	theor scaled
HO + HOH = HOH + OH (1)	1.82(−17)	1.93(−16)			
$H^{18}O$ + HOH = $H^{18}OH$ + OH (2)	2.16(−17)	2.22(−16)	(2.2 ± 1.0)(−16)	0.84	0.87
DO + HOH = DOH + OH (3)	1.79(−17)	2.05(−16)	(3 ± 1.0)(−16)	1.01	0.94
HO + DOD = HOD + OD (4)	7.12(−19)	1.50(−17)	5(−17)[b]	25.49	12.87

[a] Taken from ref 4. [b] Upper limit.

results predict the ratios $k_3/k_2 = 0.83$ and $k_4/k_3 = 0.04$, while the experimental values are $k_3/k_2 = 1.36$ (if the ranges of error of both k_2 and k_3 are not taken into account) and $k_4/k_3 < 0.17$. So, we obtain a reaction 2 that is slightly faster than reaction 3. Although this theoretical result seems to disagree with the opposite experimental result, it is compatible, in fact, with the margins of error indicated for the corresponding experimental rate constants ($\pm 1.0 \times 10^{-16}$ cm^3 molecule^{-1} s^{-1}), which could invert the actual order of rates.

On the other hand, we have to remark that, after the level of calculation was chosen, no fitting of theoretical values (apart from the scaling of UMP2 frequencies) has been done up to this point. In this way we have obtained quite acceptable rate constants and identified the main factors that govern the mechanism of these hydrogen abstraction reactions by the hydroxyl radical. To test the influence of the errors associated with the numerical values on the validity of our main conclusions, we have intended to scale the results. So, scaling the classical energy along the MEP by a factor of 0.73 we are able to accurately reproduce the experimental rate constant of reaction 2 at 300 K. Then, using this scaled MEP, we have recalculated the rate constants of the other reactions at 300 K. The corresponding results are also shown in Table 6. The scaled rates better match the corresponding experimental rates. Whatever the case may be, despite some variations in the particular numerical values, the conclusions for the mechanism of these reactions hold.

Conclusions

In this paper, we have studied the gas-phase radical−molecule identity reaction HO + HOH → HOH + OH theoretically, along with three associated isotope exchange reactions. To this end, we have used high-level electronic structure calculations plus canonical variational transition state theory including multidimensional quantum effects on the nuclear motion by the small-curvature tunneling semiclassical adiabatic ground-state approximation.

We have shown that, as both reactants approach each other, a first complex (^{2}A′ electronic state with C_s symmetry) with a hydrogen bond between the hydrogen atom of the hydroxyl radical and the oxygen atom in water is formed. Then the hydrogen abstraction itself occurs to achieve a second complex (equivalent to the first one for the perprotio reaction), which finally dissociates toward the products. Therefore, these reactions take place through several dynamical bottlenecks, although calculations based on the canonical unified statistical theory demonstrate that, at least within the range 200−700 K, the final rate constant is entirely determined by the rate constant of the abstraction bottleneck.

We have found that tunneling is very important in these hydrogen (or deuterium) transfer processes at 300 K and even at higher temperatures. The existence of the complex, which provokes a faster fall of the adiabatic potential energy moving away from the hydrogen abstraction transition state and so reduces the width of the clasically forbidden region, is the main cause for such large tunneling effects. The noticeable curvature of the theoretical Arrhenius plot over the range 200−1000 K confirms the importance of tunneling. However, a nearly linear Arrhenius plot apparently results if only a smaller range of temperature is considered (300−420 K). The activation energies and the preexponential factors of these reactions are small, in clear agreement with the experimental values, also as a consequence of tunneling.

On the other hand, we have provided reasonable theoretical values for the rate constants (which are especially useful in the case of the two reactions for which there are no well-determined experimental rate constants) for the four reactions studied, along with the corresponding kinetic isotope effects.

Finally, we have to remark that, although we are still unable to reproduce the experimental numerical values of the rate constants exactly (probably due to both theoretical and experimental uncertainties), without any kind of fitting our theoretical results are accurate enough to shed light on the intimate details of the mechanism of these gas-phase hydrogen abstraction reactions by the hydroxyl radical.

Acknowledgment. Financial support from the "Dirección General de Enseñanza Superior (DGES)" through Project PB95-0637 and the use of the computational facilities of the CESCA and CEPBA coordinated by the C^4 are gratefully acknowledged.

References and Notes

(1) Warnatz, J. In *Combustion Chemistry*; Gardiner, W.C., Jr., Ed.; Springer-Verlag: New York, 1984.
(2) Finlayson-Pitts, B. J.; Pitts, J. N., Jr. *Atmospheric Chemistry*; Wiley: New York, 1986.
(3) Atkinson, R. *Chem. Rev.* **1986**, *86*, 69 and references therein.
(4) Comes, J. F. *Angew. Chem., Int. Ed. Engl.* **1994**, *33*, 1816.
(5) Dubey, M. K.; Mohrschladt, R.; Donahue, N. M.; Anderson, J. G. *J. Phys. Chem. A* **1997**, *101*, 1494.
(6) Medhurst, L. J.; Fleming, J.; Nelson, H. H. *Chem. Phys. Lett.* **1997**, *266*, 607.
(7) Sekušak, S.; Liedl, K. R.; Rode, B. M.; Sabljić, A. *J. Phys. Chem. A* **1997**, *101*, 4245.
(8) Villenave, E.; Orkin, V. L.; Huie, R. E.; Kurylo, M. J. *J. Phys. Chem. A* **1997**, *101*, 8513.
(9) Pataki, L.; Mady, A.; Venter, R. D.; Poirier, R. A.; Peterson, M. R.; Csizmadia, I. G. *J. Mol. Struct. (THEOCHEM)* **1986**, *135*, 189.
(10) Kim, K. S.; Kim, H. S.; Jang, H. J.; Kim, H. S.; Mhin, B.-J.; Xie, Y.; Schaefer, H. F., III *J. Chem. Phys.* **1991**, *94*, 2057.
(11) Xie, Y.; Schaefer, H. F., III *J. Chem. Phys.* **1993**, *98*, 8829.
(12) Nanayakkara, A. A.; Balint-Kurti, G.-G.; Williams, I. H. *J. Phys. Chem.* **1992**, *96*, 3662.
(13) Hand, M. R.; Rodriquez, C. F.; Williams, I. H.; Balint-Kurti, G. G. *J. Phys. Chem. A* **1998**, *102*, 5958.
(14) Liu, Y.-P.; Lynch, G. C.; Hu, W.-P.; Melissas, V. S.; Steckler, R.; Garrett, B. C.; Lu, D.-h.; Truong, T. N.; Isaacson, A. D.; Rai, S. N.; Hancock, G. C.; Laurderdale, J. G.; Joseph, T.; Truhlar, D. G. *POLYRATE*, QCPE program 601-version 5.0.1; Quantum Chemistry Program Exchange: Indiana University, Bloomington, IN, 1993 (*QCPE Bull.* **1993**, *13*, 28).
(15) Frisch, M. J.; Trucks, G. W.; Schlegel, H. B.; Gill, P. M. W.; Johnson, B. G.; Robb, M. A.; Cheeseman, J. R.; Keith, T. A.; Petersson, G. A.; Montgomery, J. A.; Raghavachari, K.; Al-Laham, M. A.; Zakrzewski, V. G.; Ortiz, J. V.; Foresman, J. B.; Cioslowski, J.; Stefanov, B. B.; Nanayakkara, A.; Challacombe, M.; Peng, C. Y.; Ayala, P. Y.; Chen, W.; Wong, M. W.; Andres, J. L.; Replogle, E. S.; Gomperts, R.; Martin, R. L.; Fox, D. J.; Binkley, J. S.; Defrees, D. J.; Baker, J.; Stewart, J. P.; Head-

Gordon, M.; Gonzalez, C.; Pople, J. A. *Gaussian 94*; Gaussian, Inc.: Pittsburgh, PA, 1995.
(16) Hehre, W. J.; Radom, L.; Schleyer, P. v. R.; Pople, J. A. *Ab Initio Molecular Orbital Theory*; Wiley: New York, 1986.
(17) Frisch, M. J.; Pople, J. A.; Binkley, J. S. *J. Chem. Phys*. **1984**, *80*, 3265.
(18) Møller, C.; Plesset, M. S. *Phys. Rev*. **1934**, *46*, 618.
(19) Parr, R. G.; Yang, W. *Density Functional Theory of Atoms and Molecules*; Oxford University Press: New York, 1989.
(20) Kohn, W.; Becke, A. D.; Parr, R. G. *J. Phys. Chem*. **1996**, *100*, 12974.
(21) Becke, A. D. *J. Chem. Phys*. **1993**, *98*, 5648.
(22) Becke, A. D. *J. Chem. Phys*. **1996**, *104*, 1040.
(23) Pople, J. A.; Head-Gordon, M.; Raghavachari, K. *J. Chem. Phys*. **1987**, *87*, 5968.
(24) Scuseria, G. E.; Janssen, C. L.; Schaefer, H. F., III *J. Chem. Phys*. **1988**, *89*, 7382.
(25) Scuseria, G. E.; Schaefer, H. F., III *J. Chem. Phys*. **1989**, *90*, 3700.
(26) Gauss, J.; Cremer, C. *Chem. Phys. Lett*. **1988**, *150*, 280.
(27) Salter, E. A.; Trucks, G. W.; Bartlett, R. J. *J. Chem. Phys*. **1989**, *90*, 1752.
(28) Gonzalez, C.; Sosa, C.; Schlegel, H. B. *J. Phys. Chem*. **1989**, *93*, 2435, 8388(E).
(29) Miller, W. H.; Handy, N. C.; Adams, J. E. *J. Chem. Phys*. **1980**, *72*, 99.
(30) Garrett, B. C.; Truhlar, D. G. *J. Chem. Phys*. **1979**, *70*, 1593.
(31) Isaacson, A. D.; Truhlar, D. G. *J. Chem. Phys*. **1982**, *76*, 1380.
(32) Truhlar, D. G.; Isaacson, A. D.; Garrett, B. C. In *Theory of Chemical Reaction Dynamics*; Baer, M., Ed.; CRC Press: Boca Raton, FL, 1985; Vol. 4, p 65.
(33) Truhlar, D. G.; Kupperman, A. *J. Am. Chem. Soc*. **1971**, *93*, 1840.
(34) Fukui, K. *Pure Appl. Chem*. **1982**, *54*, 1825.
(35) Villà, J.; Truhlar, D. G. *Chem. Theor. Acc*. **1997**, *97*, 317.
(36) Garrett, B. C.; Truhlar, D. G. *J. Phys. Chem*. **1979**, *83*, 1079.
(37) Garrett, B. C.; Truhlar, D. G.; Grev, R. S.; Magnuson, A. W. *J. Phys. Chem*. **1980**, *84*, 1730.
(38) Corchado, J. C.; Espinosa-García, J.; Hu, W.-P.; Rossi, I.; Truhlar, D. G. *J. Phys. Chem*. **1995**, *99*, 687.
(39) Gonzalez, C.; Schlegel, H. B. *J. Phys. Chem*. **1990**, *94*, 5523.
(40) Hu, W.-P.; Truhlar, D. G. *J. Am. Chem. Soc*. **1995**, *117*, 10726.
(41) Hu, W.-P.; Truhlar, D. G. *J. Am. Chem. Soc*. **1996**, *118*, 860.
(42) Garrett, B. C.; Truhlar, D. G. *J. Am. Chem. Soc*. **1979**, *101*, 4534.
(43) Garrett, B. C.; Truhlar, D. G. *J. Am. Chem. Soc*. **1979**, *101*, 5207.
(44) Tucker, S. C.; Truhlar, D. G. In *New Theoretical Concepts for Understanding Organic Reactions*; Bertrán, J., Csizmadia, I. G., Eds.; Kluwer Academic: Dordrecht, 1989; p 291.
(45) Truhlar, D. G.; Isaacson, A. D.; Skodje, R. T.; Garrett, B. C. *J. Phys. Chem*. **1982**, *86*, 2252.
(46) Steckler, R.; Hu, W.-P.; Liu, Y.-P.; Lynch, G. C.; Garrett, B. C.; Isaacson, A. D.; Melissas, V. S.; Lu, D.-h.; Truong, T. N.; Rai, S. N.; Hancock, G. C.; Laurderdale, J. G.; Joseph, T.; Truhlar, D. G. *Comput. Phys. Commun*. **1995**, *88*, 341.
(47) Corchado, J. C.; Chuang, Y.-Y.; Fast, P. L.; Villà, J.; Coitiño, E. L.; Hu, W.-P.; Liu, Y.-P.; Lynch, G. C.; Nguyen, K. A.; Jackels, C. F.; Gu, M. Z.; Rossi, I.; Clayton, S.; Melissas, V. S.; Steckler, R.; Garrett, B. C.; Isaacson, A. D.; Truhlar, D. G. *POLYRATE*; version 7.9.1; University of Minnesota: Minneapolis, 1998.
(48) Corchado, J. C.; Coitiño, E. L.; Chuang, Y.-Y.; Fast, P. L.; Truhlar, D. G. *J. Phys. Chem. A* **1998,** *102*, 2424.
(49) Villà, J.; González-Lafont, A.; Lluch, J. M.; Bertrán, J. *Mol. Phys*. **1996**, *89*, 633.
(50) Lu, D.-h.; Truong, T. N.; Melissas, V. S.; Lynch, G. C.; Liu, Y.-P.; Garrett, B. C.; Steckler, R.; Isaacson, A. D.; Rai, S. N.; Hancock, G. C.; Lauderdale, J. G.; Joseph, T.; Truhlar, D. G. *Comput. Phys. Commun*. **1992**, *17*, 235.
(51) Liu, Y.-P.; Lynch, G. C.; Truong, T. N.; Lu, D.-h.; Truhlar, D. G.; Garrett, B. C. *J. Am. Chem. Soc*. **1993**, *115*, 2408.
(52) Truong, T. N.; Duncan, W. T.; Bell, R. L. *ACS Symp. Ser*. **1996**, *629*, 85.
(53) Scott, A. P.; Radom, L. *J. Phys. Chem*. **1996**, *100*, 16502.
(54) Truhlar, D. G.; Garrett, B. C. *J. Am. Chem. Soc*. **1989**, *111*, 1232.